Vortex interactions with a high-lift airfoil in a low speed wind tunnel

S. Klein*, D. Hahn†, P. Scholz‡ and R. Radespiel§
Technische Universität Braunschweig, 38108 Braunschweig, Germany

This publication describes experimental investigations on the effects of large scale disturbances on a two element airfoil. Quasi two-dimensional transversal vortices are created in a closed test-section shortly after the nozzle. Convecting along the test section, these vortices interact with the two-element airfoil in high lift configuration. Various measurement techniques, like Particle Image Velocimetry (PIV), time resolving static pressure measurements, time averaged measurements of the static pressure distribution of the high-lift airfoil and oilflow visualizations were utilized to identify and characterize these complex interactions. As a result, the influence of the induced vortices on the time resolving static pressure along the airfoil's surface is described. Moreover the vortex interaction with the airfoil flap flow is discussed.

Nomenclature

hl	=	high-lift airfoil
vg	=	vortex generator
c_{vg}	=	chord of vortex generator airfoil
c_{hl}	=	chord of high-lift airfoil
α_{hl}	=	angle of attack of high-lift airfoil
α_{vg}	=	angle of attack of vortex generator airfoil
c_p	=	static pressure coefficient
$c_{l,p}$	=	lift coefficient
u	=	x-component of velocity
w	=	z-component of velocity
M/E	=	main element of the high-lift airfoil
L/E	=	leading edge
T/E	=	trailing edge

I. Introduction

Aircraft move within an atmospheric, turbulent boundary layer. Especially during high-lift periods, e.g. landing and take off, atmospheric disturbances can have a strong impact on them. As atmospheric disturbances are predominantly three-dimensional and have a high range of frequencies, their effect on aircraft lift is very difficult to predict. Looking at a more advanced design of future high-lift systems, these critical periods of flight and the interactions between atmospheric eddies or gusts and the flow around the airfoil, respectively around the aircraft need to be understood. To date, neither the computational simulation of a flight of an airplane in atmosphere, nor the experimental simulations of atmospheric disturbances in a wind tunnel are fully feasible.

As part of the research project FOR 1066, the Technische Universität Braunschweig performs experimental investigations to establish a high quality database[3] of the behavior of a DLR-F 15 high-lift airfoil[14] in disturbed flow.[4] Within this research project the philosophy is, to start from a simple problem and proceed to more sophisticated ones. Therefore, the investigation of the interdependency of disturbances and lift is initiated by quasi two-dimensional flow conditions. Transversal quasi two-dimensional vortices, representing atmospheric up- and down-winds[5], were identified as a reasonable starting point.[7] Single vortices in a vertical plane can be created and investigated with manageable effort. Basically, experimenters have two possibilities to investigate

* Research Scientist, Institute of Fluid Mechanics, Hermann-Blenk-Str. 37, 38108 Braunschweig, simon.klein@tu-bs.de.
† Research Scientist, Institute of Fluid Mechanics, Hermann-Blenk-Str. 37, 38108 Braunschweig.
‡ Head of Research Group "Measurement and Manipulation of Flows", Institute of Fluid Mechanics, Hermann-Blenk-Str. 37, 38108 Braunschweig.
§ Professor and Head of Institute, Institute of Fluid Mechanics, Hermann-Blenk-Str. 37, 38018 Braunschweig.

objects in disturbed flow. Either specific flow distortion is introduced upstream of the object (e.g. turbulence grid[13], flexible wings/flaps[9,2], or the object that is under investigation is moved in a way, that the flow around it results in the required phenomena (e.g. helicopter rotor research[10]).

To meet the requirements of high reproducibility, specific flow distortions were produced upstream of the airfoil being under investigation. In order to keep more options in the creation of the disturbances, e.g. size intensity or sequence, an active method of flow control was chosen as described in Chapter II. For a short discussion on the selection process of methods to produce generic atmospheric disturbances in a test setup refer to Ref. 5. Chapter III describes the conducted investigations and their results. Finally a conclusion and an outlook to future investigations are given in chapter IV.

II. Experimental setup

Although transversal quasi two-dimensional vortices were identified as representative disturbances that can be produced and investigated with manageable effort, it is still a challenge to produce them reproducible and variable in a closed wind tunnel test-section.

Figure 1 displays the test setup used for the present research in principle. It includes a vortex generator airfoil and a high-lift airfoil. This publication gives only a short overview of the hardware setup and its design. For a more detailed description refer to Ref. 5.

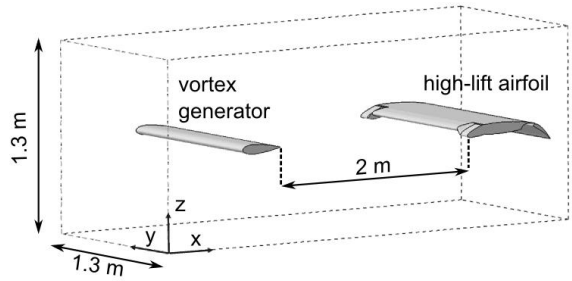

Figure 1. Assembly sketch of the vortex generator and the high-lift airfoil in the test-section.

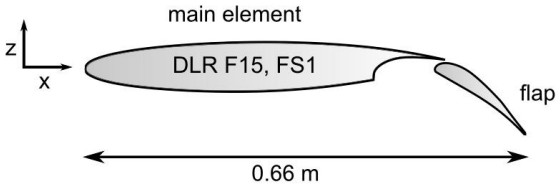

Figure 2. Contour sketch of the two-element high-lift airfoil DLR-F15.

A pitching NACA 0021 airfoil (vortex generator airfoil, chord length c_{vg} = 0.3 m), is used to create quasi two-dimensional transversal vortices. As the vortex generator airfoil varies its angle of attack, it changes its circulation and a turbulent layer of vorticity is created in its wake, see fig. 3. Whether the turbulent shear layer rolls up into a start/stop-vortex or not, is triggered by the pitch time Δt. Δt also determines the spatial dimensions of the created disturbances. The created vorticity[11] or the vortex circulation respectively is defined by the change in angle of attack α_{vg}. To create a series of start/stop-vortices, the vortex generator needs to accelerate out of and into stagnation with a certain time of hold between each pitch. In this publication a change in angle of attack of $\Delta\alpha_{vg} \approx 10°$ was performed with an average pitching velocity of 0.7 °/ms. Using these parameters, start/stop-vortices of reasonable size and vorticity could be created. Between each change in angle of attack, a stagnation period of 0.2 s completed the pitch cycles[5]. This results in a duty cycle of the vortex generation of 7.5 %.

To obtain this motion, a light-weight vortex generator airfoil is driven by a fast actuation pitching unit, based on digital linear actuation. Altogether four linear servo actuators of the type Copley XTA 3806 are arranged in pairs on each side of the vortex generator airfoil shown in fig. 4. The parallel operation of the four actuators is synchronized by a master-slave control system. Several different digital and mechanical means detect possible failure modes of the operating system and therefore prevent it from too large or asynchronous motion or excessive mechanical loads. Detailed descriptions of the fast-actuation pitching system as well as the properties of the generated vortical disturbance are given in Ref. 4, 5.

Investigations were performed in the Modell Unterschall-Windkanal Braunschweig[5] (MUB), a low-speed wind tunnel with a test-section of 1.3m x 1.3m x 6m. A DLR-F15 contoured two-element airfoil model was used in high-lift configuration (FS#1 configuration[5], chord length c_{hl} = 0.6 m), see fig. 2, to investigate its interactions with the vortices created upstream. Local sidewall droop-noses are integrated into the high-lift airfoil, as displayed in fig. 1, to investigate a relatively large model in a relatively small test-section.[3] These local, small devices (10% span) prevent sidewall boundary layer induced separations.[3,14]

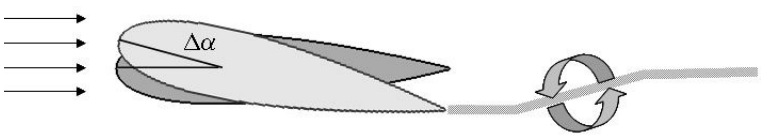

Figure 3. Sketch of the vortex generator functionality

Figure 4. Pair wise arrangement of the linear servo actuators on the side of the light-weight vortex generator airfoil.

The distance between the vortex generator trailing edge and the leading edge of the high-lift airfoil is 2 m. Moreover the vortex generator airfoil and the high-lift airfoil are located at the same height.

55 pressure taps in the center plane of the main element and 30 taps in the center plane of the flap, so as 2 x 20 taps along two outer sections serve for time averaged static pressure measurements. A PSI 8400 SDI multi-channel pressure scanner with a full scale output accuracy of 0.05 % was used to acquire the data. The PSI pressure scanner offers a sampling frequency of 5 Hz. Every measurement point represents an average on 100 samples. All presented lift curves are uncorrected integrals of the static pressure measurements, which means $c_{l,p}$ over α_{hl}.[1] No wind tunnel corrections are applied. For time resolving pressure measurements Kulite® XCQ 93 and LQ 62 sensors, integrated in the airfoil's surface and trailing edges, are used. Both types of Kulite sensors have a full scale output accuracy of 0.1 %. For sampling the data M2i4652 Spectrum acquisition cards with 2GSample memory onboard and max. 3 Ms/s sampling rate are used. Kulite measurements are conducted with a sampling frequency of 50 kHz for more than 40 seconds. Thus, more than 80 pitch cycles of the vortex generator are captured. During post-processing the Kulite data are phase-locked and ensemble averaged on the number of pitch cycles captured. Phase-locked PIV measurements are triggered by a photo sensor, mounted to an actuator of the vortex generator drive. This sensor is adjusted so that a trigger pulse is given when the vortex generator moves out of stagnation. Due to mechanical deviations among different experimental entries and due to electric jitter, the uncertainty of the trigger signal is approximately 2 milliseconds. One to two Litron Nano T double pulse lasers with a wavelength of 532 nm are used depending on the size of the investigated area. A LaVision Imager Pro X 11M camera with a Zeiss Macro-Planar T 2/50 lens and LaVision's DaVis 7 software are used for acquisition and evaluation of the data. A programmable timing unit (PTU) by LaVision allowed reliable triggering of lasers, camera and the motion of the vortex generator. The accuracy of the PTU is around 5 ns. Each time series includes 300 double pictures and after the evaluation process the spatial resolution is 2 mm (for more details see Ref. 5). Droplets of an average size of 1 µm of DEHS seeding[8] are injected into the wind tunnel settling chamber. Oilflow visualizations are conducted to investigate the boundary layer along the high-lift airfoil. To avoid damages of the sensors in the airfoil's center plane, these visualizations are carried out 300mm parallel to it. Since previous results showed that the two-dimensionality of the flow is fulfilled well, these visualizations can be compared to results in the center plane of the airfoil.[6]

To achieve a Reynolds number of $Re = 2 \times 10^6$ at the high-lift airfoil, the free stream velocity is adjusted to 50 m/s.

III. Results

In this chapter, measurements of the high-lift airfoil interacting with the upstream created vortices and their interpretation will be presented. The pitch cycle of the vortex generator described in section II generates vortices that yield peak-to-peak induced angles of attack of approximately 5°. The characteristics of the vortices in an otherwise empty test-section and their detailed evolution and convection are not part of this publication. Detailed information on these topics can be found in Ref. 4 and 5.

A. Vortex-influence on the airfoil's static characteristics

The static characteristics of the high-lift airfoil, like the lift curve $c_{l,p}(\alpha_{hl})$ and the static pressure distribution $c_p(x)$ are the first quantities to be considered for the investigation of the vortex-airfoil interaction. An extensive discussion of the high-lift airfoil characteristics under steady conditions has been given in Ref. 6 and will not be part of this work. An impression of how the induced disturbances of the vortex influence the high-lift airfoil lift curve can be obtained in fig. 5. The static pressure data is measured by full runs from negative angles of attack up beyond stall. Doing so, the data are acquired after the corresponding angle of attack was adjusted. The intervals of the various angles of attack range from $\Delta\alpha_{hl} = 2°$ in the linear region of the lift curve to $\Delta\alpha_{hl} = 0.3°$

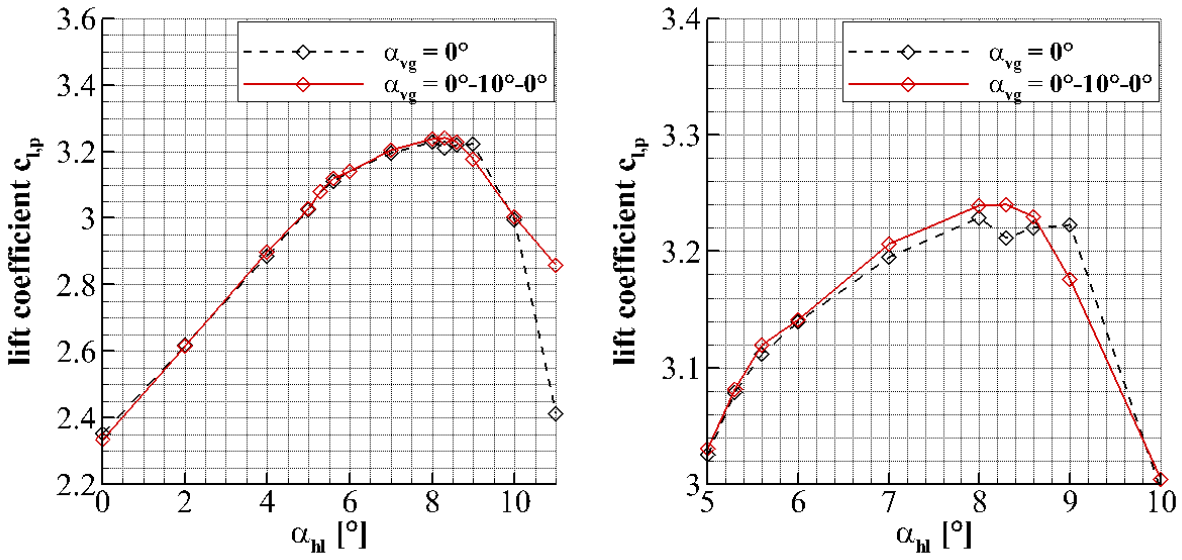

Figure 5. (a) Lift coefficient $c_{l,p}$ over high-lift airfoil angle of attack α_{hl} for undeflected vortex generator (α_{vg} = 0°) and for dynamically moving vortex generator (α_{vg} = 0°-10°-0°). (b) close-up of (a) around region maximum lift region.

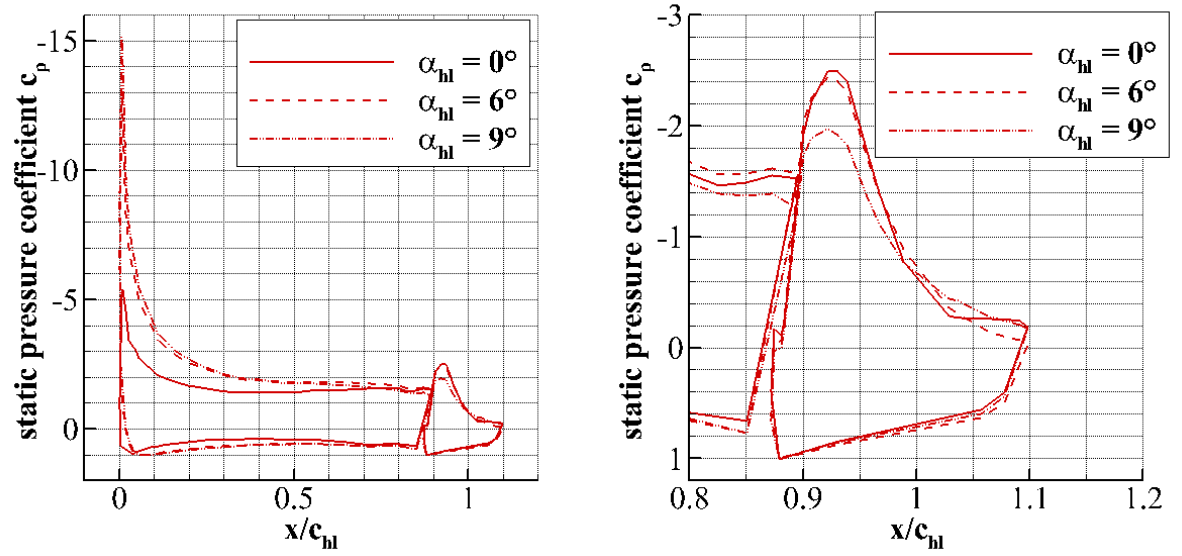

Figure 6. (a) static pressure distribution along the high-lift airfoil's surface (b) close up of the distribution on the airfoil's flap.

close to maximum lift. For each angle of attack, integration of the static pressure distribution yields a lift coefficient. This process is conducted for both the undeflected vortex generator with α_{vg} = 0° and for the dynamically moving vortex generator, to investigate the influence of the induced vortex on the lift curve. In the linear region of fig. 5, between α_{hl} = 0° and α_{hl} = 5°, the two curves coincide well. At α_{hl} = 5° viscous effects start to dominate the characteristics. Consequently the slope of both curves decreases. From this point, the lift curves differ slightly, where the dynamically disturbed case results in slightly higher lift coefficients. At the point of maximum lift, the difference is roughly $\Delta c_{l,p}$ = 0.02. At angles of attack beyond α_{hl} = 8.3°, both lift curves show stall. However, it can be highlighted that due to the low duty cycle of the vortex generation of 7.5 % the dynamical disturbance of the generated vortex has a vanishing influence on the averaged static pressure distribution. To investigate the dynamics of the disturbance, time resolving measurement techniques are needed.

Before presenting time resolving data, the static pressure distribution of the high-lift configuration shall be investigated in more detail. Hence, a discussion of the dominant high-lift effects is addressed. As examples, fig.

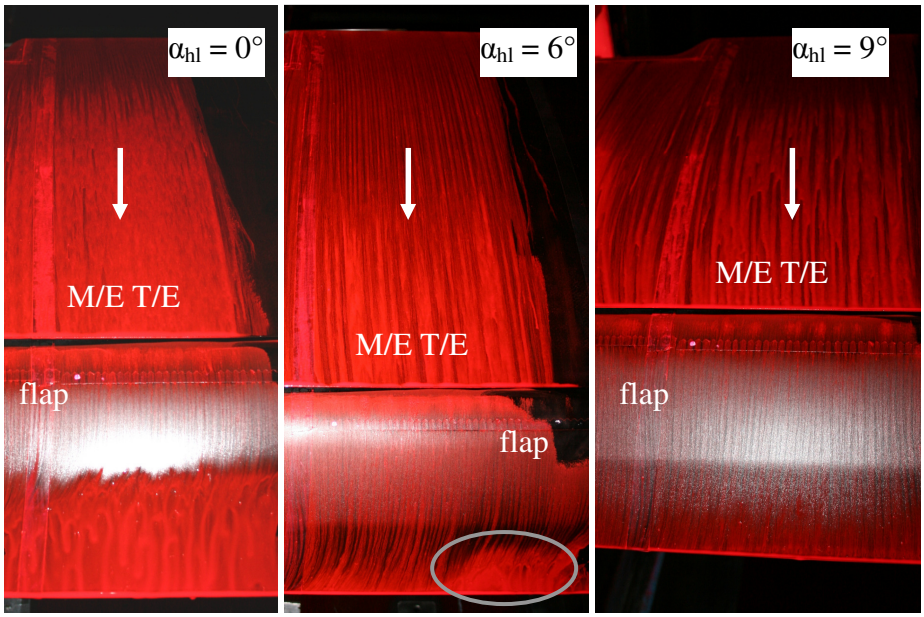

(a) **(b)** **(c)**

Figure 7. Oilflow visualizations of the flap for varying angle of attack. (a) α_{hl}=0°, (b) α_{hl}=6°, (c) α_{hl}=9°.

6 shows the static pressure along the airfoil's surface for three angles of attack, namely α_{hl} = 0°, 6° and 9°. Since the differences in $c_{l,p}$ for the undisturbed and disturbed conditions are small (see fig. 5), only the static pressure distributions of the disturbed case are considered.

Looking at the main element, the leading edge suction peak rises with increasing angle of attack. The flow phenomena of the main element trailing edge and the flap require some explanations. For α_{hl} = 0° the flap is detached. Indications for this phenomenon are the region of constant c_p close to the flap's trailing edge and the negative c_p at the trailing edge. At α_{hl} = 6°, growing circulation of the main element reduces the suction peak of the flap. More important, growing main element circulation causes the reattachment of the flap's trailing edge flow. A continuous increase of c_p along the flap's upper surface can be observed together with a trailing edge c_p tending to positive values. These findings indicate that the separation of the flap flow is reduced.[14] Whether the flap is completely attached at this angle of attack or not, is difficult to deduce from the static pressure distribution only. More data will be considered below to resolve this finding. At this point of investigations, we remind of the fundamental effects of high-lift aerodynamics to understand the characteristics of the present high-lift configuration in general. The predominant effect of this configuration is the "circulation effect", described by A.M.O. Smith.[12] A sketch of this effect is given in fig. 8. In Ref. 12, Smith described five primary effects of high-lift configurations, among these there is the "circulation effect". Concerning this effect, Smith stated that the circulation of the flap effectively places the trailing edge of the main element at a higher angle of attack as compared to the airfoil without flap. Since the Kutta condition is still met the circulation of the main element must increase. As the global angle of attack increases, the growing circulation of the main element leads to a downwash at the flap. This effect places the flap at an effectively lower angle of attack. Consequently, the flap suction peak is reduced, the pressure gradient is smaller (less load) and the flap remains attached along its upper surface. Hence, this is a system of reciprocal interference as the main element's circulation also influences the flap flow.

Moreover, another effect described by Smith in Ref. 12, the "dumping effect", is observable for the present high-lift configuration. Accordingly, the flap's circulation likewise increases the velocity at the main element trailing edge in tangential direction. Thus, the static pressure is reduced. This condition is favorable to the boundary layer. The suction side static pressure distribution can be likewise reduced for the same separation margin.[12]

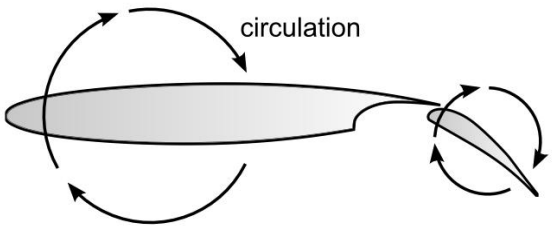

Figure 8. Sketch of the circulation effect in high-lift configurations with main element and flap, according to Ref. 12.

Comparing these explanations to the discussion of fig. 6, both effects are evident. As oilflow visualization in fig. 7a shows, at α_{hl} = 0° the flap is

heavily loaded and flow separation can be observed. Increasing the angle of attack to $\alpha_{hl} = 6°$, the main element trailing edge pressure is reduced. This indicates a higher velocity due to the "dumping effect" of the flap. Furthermore, the reduced suction peak of the flap and the partially attached flow further downstream show the influence of the main element circulation on the flap due to the "circulation effect". Again, these results coincide with the oilflow visualization in fig. 7b, where attached flow characteristics can be observed, and only partial separations occur (see the grey oval).

Increasing the angle of attack beyond maximum lift to $\alpha_{hl} = 9°$, the airfoil flow is close to stall (see fig. 5). In contrast to the main element suction peak, which is further increased, the flap's suction peak is decreased (see fig. 6). Observable is the reduced flap circulation which results in the increased pressure at the main element trailing edge. The oilflow visualization in fig. 7c shows regions of beginning separation at the main element trailing edge that underline the near stall character of the high-lift airfoil at this angle of attack.

To conclude, the results of the static pressure distributions and the oilflow visualizations coincide and are in good agreement with previous entries.[6] Moreover, the distinct angles of attack chosen serve as good examples for the flow around the high-lift airfoil. Further considerations at these angles of attack allow a broad overview of the vortex interaction on the different flow phenomena. To remind these phenomena, a summary of the previous discussion is given. At $\alpha_{hl} = 0°$, the main element has an attached flow and the flap is heavily loaded

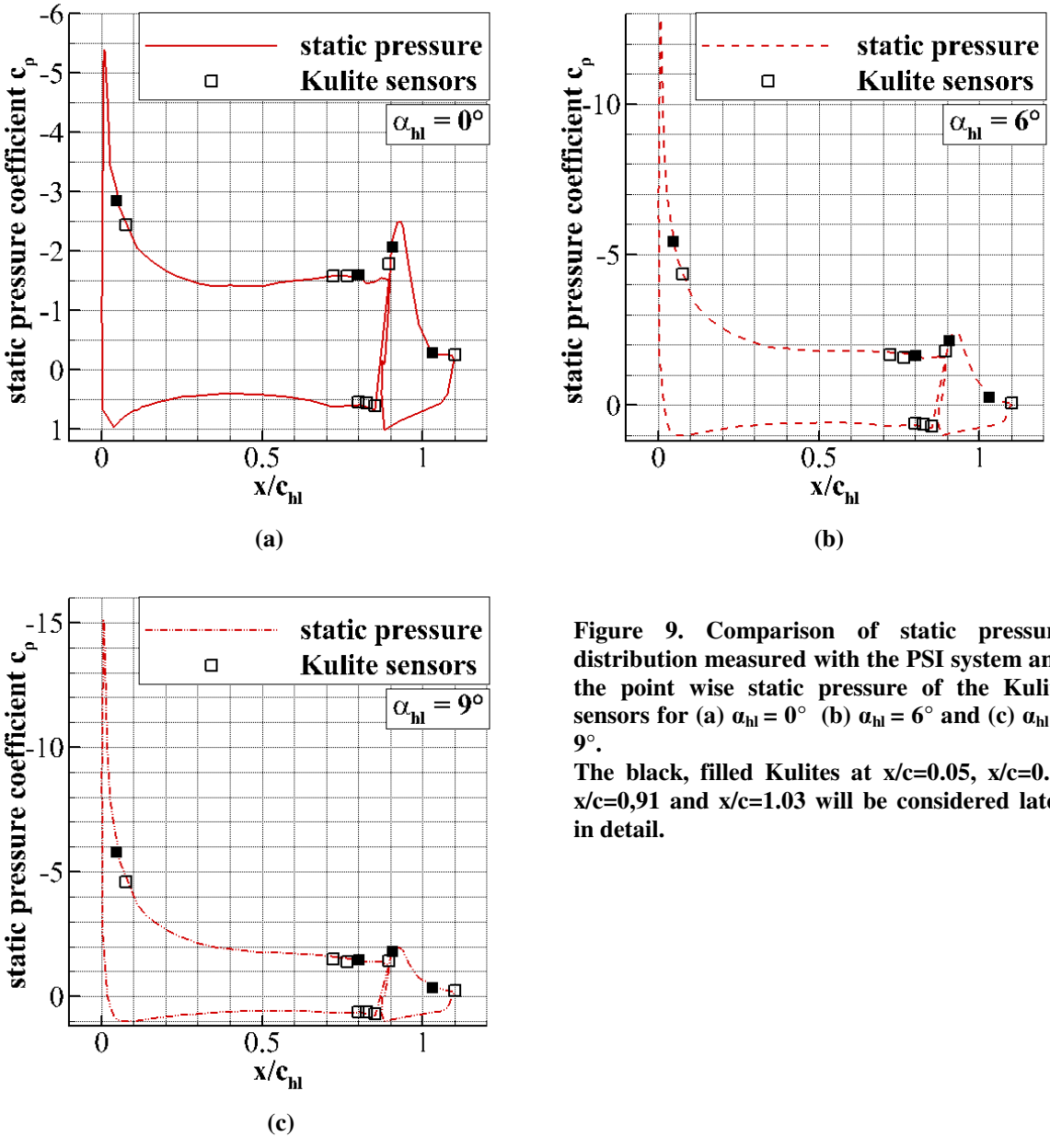

Figure 9. Comparison of static pressure distribution measured with the PSI system and the point wise static pressure of the Kulite sensors for (a) $\alpha_{hl} = 0°$ (b) $\alpha_{hl} = 6°$ and (c) $\alpha_{hl} = 9°$.
The black, filled Kulites at x/c=0.05, x/c=0.8, x/c=0,91 and x/c=1.03 will be considered later in detail.

and shows large separation. With higher angle of attack, as can be seen at $\alpha_{hl} = 6°$, the main element circulation forces the flap to attach. Only local separations occur at $\alpha_{hl} = 6°$. Beyond the angle of maximum lift, at $\alpha_{hl} = 9°$, separation effects can be observed close to the main element trailing edge. The flow characteristics are influenced by the near stall effects.

The next step of investigation is the discussion of time resolving static pressure data. These data are acquired with the Kulite sensors along the airfoil's surface. First, the Kulite signals are compared to the existing static pressure distributions. Thereby it is verified that the Kulite sensors yield reasonable data. Altogether 12 Kulite sensors are integrated along the center plane of the airfoil and at the leading edges. Five Kulites are located on the main element upper side, three Kulites in the cove on the lower side, two Kulites on the flap and one Kulite on the main element trailing edge and on the flap's trailing edge, respectively. The accurate positions can be found in fig. 9. Kulite data are acquired for more than 40 seconds with a sampling frequency of f = 50kHz. This results in approximately 2 million data points and more than 80 pitch cycles of the vortex generator. After acquisition the data are phase-locked and ensemble-averaged on the number of pitch cycles. For the comparison of Kulite data with the static pressure distribution, a second average on the ensemble-averaged Kulite signal is conducted, resulting in one value for each sensor. Figure 9 presents the comparison for the three angles of attack $\alpha_{hl} = 0°$, 6° and 9°. Small differences can only be observed close to the main element trailing edge and on the pressure side of the airfoil. Nevertheless, the averaged results of the Kulite sensors are in good agreement with the static pressure distribution.

B. Vortex disturbance at the main element leading edge

In this section, the dynamics of the airfoil-vortex interaction at the main element leading edge will be considered in detail. Figure 10 shows the time traces of the Kulite sensor located at the main element leading edge at x/c=0.05 (see also fig. 9). The Kulite data shown here are the results of the ensemble average on more then 80 pitch cycles of the vortex generator. The point t = 0s equals the start of the vortex generator. Again, representatively for the entire angle of attack spectrum, the angles $\alpha_{hl} = 0°$, 6° and 9° are shown.

From fig. 10, it becomes clear that the magnitude of disturbance at the main element leading edge is rather independent of the angle of attack. Furthermore, the starting point and the point of maximal disturbance are likewise independent of the angle of attack. These results are in good agreement with previous findings in Ref. 6. Moreover, the three signals show two peaks. First a pronounced decrease of static pressure, followed by a slight increase of static pressure. In this context, remember the functionality of the vortex generator in fig. 3. Consider the vortex reaching the high-lift airfoil. For reasons of simplicity, the part of the vortex reaching the high-lift airfoil first is called the leading flank of the vortex. The trailing flank of the vortex specifies the upstream part of the vortex. The leading flank of the vortex effectively induces a higher angle of attack, whereas the trailing flank of the vortex induces a lower angle of attack. Therefore, fig. 10 indicates that the main element leading edge Kulite measures both the leading and the trailing flank of the vortex. However, the trailing flank of the generated vortex seems to be damped. Previous, time resolving 5-hole-probe pressure measurements in the flow show a symmetric signature of the generated vortex in a test section without high-lift airfoil.[4] With the high-lift airfoil mounted in the test section, time resolving 5-hole-probe pressure measurements in the flow show the damping of the trailing flank signature of the vortex.[6] Therefore, it is a satisfactory result that the main element leading edge Kulite likewise measures this signature and reproduces the damping of the vortex' trailing flank.

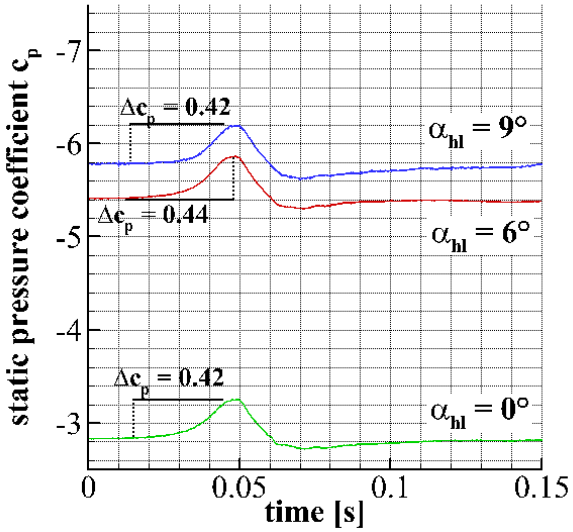

Figure 10. Kulite data at the main element leading edge. The Kulite is located at x/c=0.05 (see also fig. 9).

To investigate the reaction of the leading edge static pressure on the generated vortex in a deeper sense, we access the flow field around the high-lift airfoil measured with PIV. Figure 11 shows the phase-locked velocity field at the leading edge of the main element and at the flap for $\alpha_{hl} = 0°$. The contour and vector plot at the leading edge correspond to the instant t = 50ms after the start of the vortex generator, whereas the flap flow represents the instant t = 58ms. The background contour plot depicts the $(u,w)^T$-velocity-field. The vectors in the foreground are the results of the so called "difference velocity field method".[5] The "difference vector field

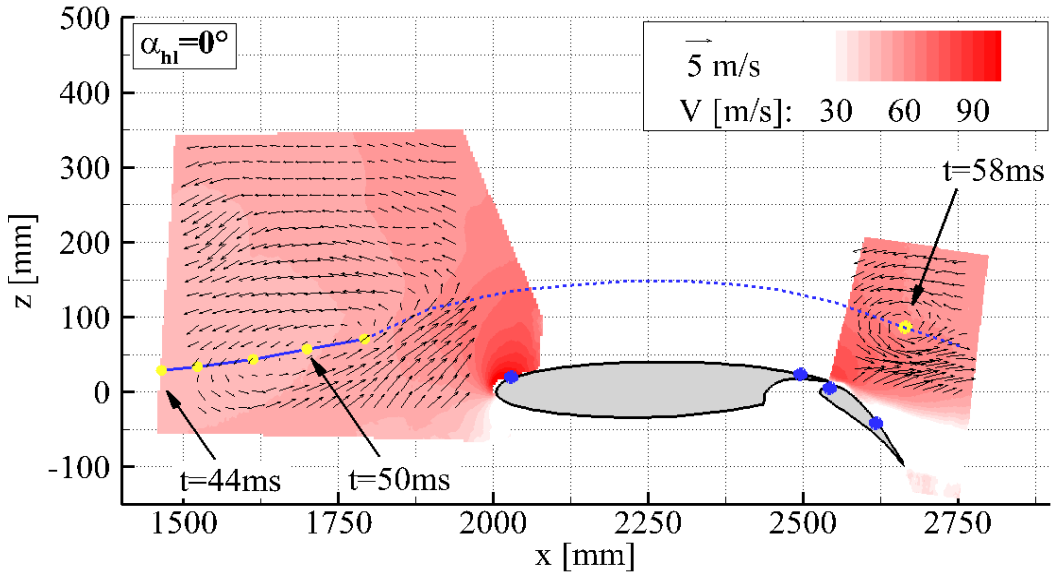

Figure 11. Passing of the generated vortex around the high-lift airfoil for α_{hl}=0°. The yellow circles depict the position of the vortex center found in the PIV recordings. The solid blue line is the trace of the vortex core, whereas the dashed blue line approximates the trace of the vortex. The blue circles on the airfoil mark the position of the Kulite sensors that are discussed in detail (x/c = 0.05, x/c = 0.80, x/c = 0.91 and x/c = 1.03). The PIV data at the main element leading edge are captured at t = 50ms. The data at the airfoil's flap depicts time t = 58ms.

method" subtracts the velocity field with static deflected vortex generator (α_{vg} = 10°) from the phase-locked velocity field with dynamically moving vortex generator. This method will be discussed in detail later. At this point, we are satisfied with the result that the "difference vector field method" has proven to be able to show the presence of the generated vortex.[5] For different points in time, the difference vector field method is used to detect the core of the generated vortex. The results are represented by the yellow circles in front of the main element and at the flap. The time interval between the circles at the main element leading edge are Δt = 2ms. The circulation of the airfoil causes a stretching of the vortex close to the main element's leading edge. Therefore, the vortex core could not be defined for instants later than t = 52ms. The trace of the vortex between t = 52ms and t = 58ms is approximated by the dashed, blue line. Moreover, fig. 11 shows the position of the main element leading edge Kulite as a blue circle. The three additional Kulites close near to the trailing edge will be considered later.

Let's return to the influence of the generated vortex on the leading edge static pressure. From fig. 10, we learnt that the maximum magnitude of disturbance appears at approximately time t ≈ 50ms for all three angles of attack. Considering fig. 11, it is evident that the vortex core is roughly 250mm in front of the main element at time t = 50ms. Hence, the strongest disturbance of the static pressure appears although the vortex core has not reached the main element. This is an indication that the static pressure at the main element leading edge is mainly influenced by the effective change of the angle of attack that arises from the leading and trailing flank of the generated vortex. Hence, this result underlines the findings of fig. 10. Finally, another effect can be observed in fig. 10. The disturbance of the vortex' trailing flank remains visible in the pressure signal approximately until time t = 100ms. This time even increases with higher angle of attack. Viscous effects that are predominant at angles of attack above α_{hl}= 5° (see fig. 5) might be the reason for the delayed relaxation back to the undisturbed level of static pressure.

C. Vortex disturbance along the high-lift airfoil for α_{hl} = 0°

In this section, we consider further time resolving Kulite data. Thereby, it can be investigated whether the generated vortex has the same effect along the high-lift airfoil as observed for the main element leading edge or not. In addition to the main element leading edge Kulite at x/c = 0.05, the data of three other Kulites are used. These Kulites are located close to main element trailing edge (x/c = 0.80), at the flap's leading edge (x/c = 0.91) and close to the flap's trailing edge (x/c = 1.03), respectively. To allow a better comparison of the different Kulite signals, a reduced time trace of the pressure signal is calculated for each Kulite. This is done by subtracting the static pressure of the undisturbed case at time t = 0s of each Kulite from its ensemble averaged time trace. Figure 12 shows these reduced signals of the four Kulites for α_{hl} = 0°.

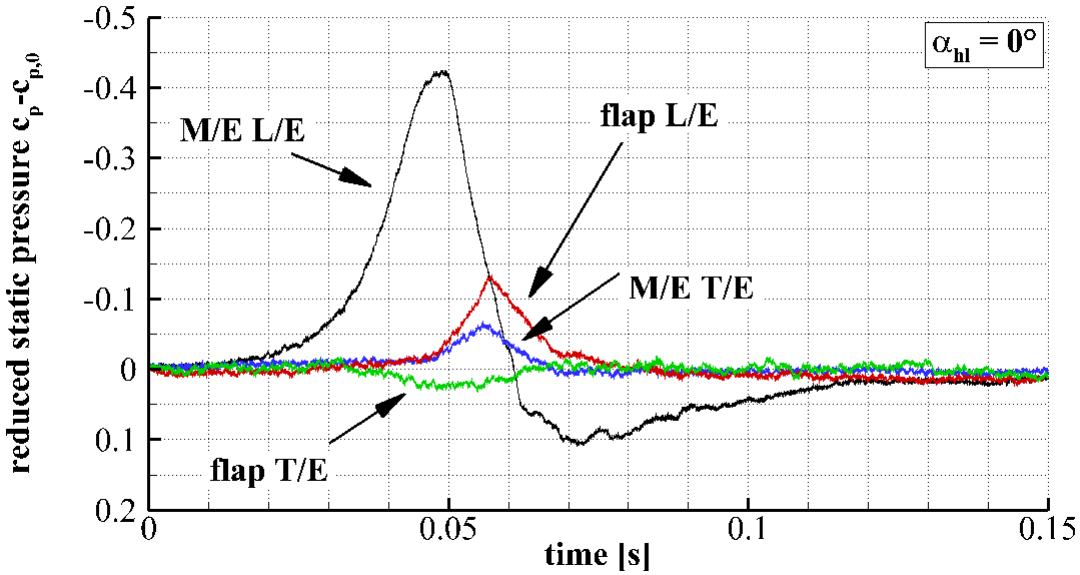

Figure 12. Time traces of the reduced static pressure, $c_p(t)$-$c_p(t=0)$, of four Kulites along the airfoil's surface for α_{hl} = 0°. The Kulites are located close to the main element leading edge (x/c=0.05) and trailing edge (x/c=0.80), and close to the flap's leading edge (x/c=0.91) and trailing edge (x/c=1.03).

To approach these results, we start with the signal of the main element leading edge Kulite to remind the effects observed in the previous section. The main element leading edge is sensitive to both the leading and trailing flank of the vortex, whereas the effect of the trailing flank is damped. Before investigating the signals of the other three Kulites, this is a good moment to remind the flow characteristics of the three angles of attack, that were discussed in section A in detail.
This is helpful for a better understanding of the disturbance of the generated vortex on the different Kulite signals.

- α_{hl}=0° : Attached flow on the main element and high loading of the flap's boundary layer that causes separation.
- α_{hl}=6° : Attached flow on the main element and almost entirely attached flap flow due to the circulation effect. Partial separation regions can occur.
- α_{hl}=9° : Beyond maximum lift. Flow characteristics are dominated by near stall effects.

Based on that, the disturbance on the four Kulite signals and their behavior with respect to each other can be discussed. The three Kulites further downstream from the main element leading edge only measure either a pressure decrease or a pressure increase. This reaction is different to that of the main element leading edge Kulite. However, one can observe that the main element trailing edge and the flap's leading edge react similarly. Like the main element leading edge, they show a distinct pressure decrease. The maximum magnitude of disturbance is located approximately at time t = 0.57ms. Moreover the temporal start of the disturbance is more or less the same for both Kulites and they return to the undisturbed level more or less at the same time. A different behavior can be noticed for the flap's trailing edge Kulite. In contrast, it shows a slight pressure increase. Moreover, its signal gets disturbed before the disturbance reaches the two Kulites located upstream. Interestingly, the appearance of the maximum disturbance coincides rather with the signal of the main element leading edge Kulite. Therefore it must be concluded that the reaction of the flap trailing edge is closely related to the reaction of the main element leading edge. However, it only seems to be sensitive to the positive induced angle of attack. Since the trailing edge of the flap is heavily loaded and thus separated at this angle of attack, we assume that this phenomenon plays an important role for the pressure reaction of the flap trailing edge.

To investigate the above mentioned findings on the airfoil's flap, we consider phase-locked PIV results, measured at this position. To get an impression of the dynamics on the airfoil's flap, fig. 13 shows an exemplary time series of the processed PIV data for α_{hl} = 0°. In the background a contour plot of the $(u,w)^T$-velocity-field is presented, whereas the vectors in the foreground result from the "difference vector field method".[5] As mentioned in section B, the "difference vector field method" subtracts the velocity field with static deflected vortex generator (α_{vg} = 10°) from the phase-locked velocity field with dynamically moving vortex generator. It is used to identify the generated vortex in the vector field of the PIV measurements. Before discussing the results in fig. 13 in detail, a small excursus about the "difference vector field method" is made.

Previous investigations showed that common vorticity-detection methods yield insufficient results due to shear effects on the generated vortex caused by the high-lift airfoil circulation.[5] An alternative approach to detect the generated vortex is the "difference vector field method". Worth to mention, this method has to be used carefully. Two velocity fields with large magnitudes are subtracted from each other to indicate the presence of the induced vortex with a velocity magnitude one order smaller. Therefore this method is sensitive to the quality of the mean velocity fields used. Nevertheless, the "difference vector field method" has proven to be able to show the presence of the generated vortex.[5] To support the ability of the "difference vector field method", the common λ2-vorticity-criterion is applied on the $(u,w)^T$-velocity-field of time t = 0.058s in fig. 14b. This criterion computes the Hessian-matrix of the local pressure. A negative, second eigen value of this matrix is an indication for vortex regions in the investigated velocity field. Since the upper limit of the contour plot in fig. 14b is zero, it can be noticed that the core of the vortical structure detected by the λ2-criterion coincides with the results of the "difference vector field method". Hence, the "difference vector field method" is assumed to yield reasonable results.

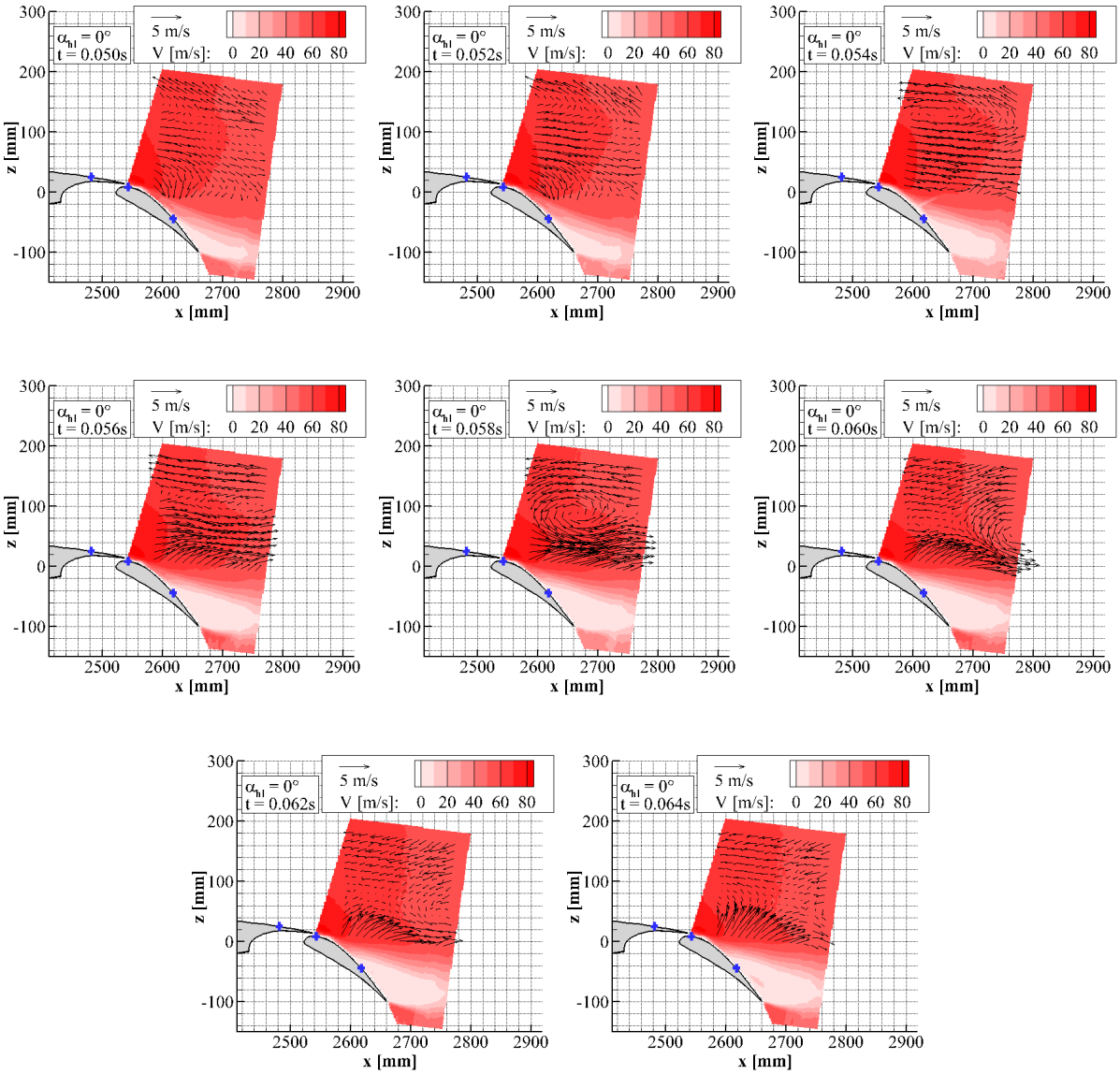

Figure 13. Temporal evolution of the flow field on the high-lift airfoil's flap. The period starts at t = 0.05s and ends at t = 0.064s with intervals of 0.002s. In the background, a contour plot of velocity $(u,w)^T$ is shown. The vectors stem from the "difference velocity field method". The Kulite positions are marked by the blue crosses.

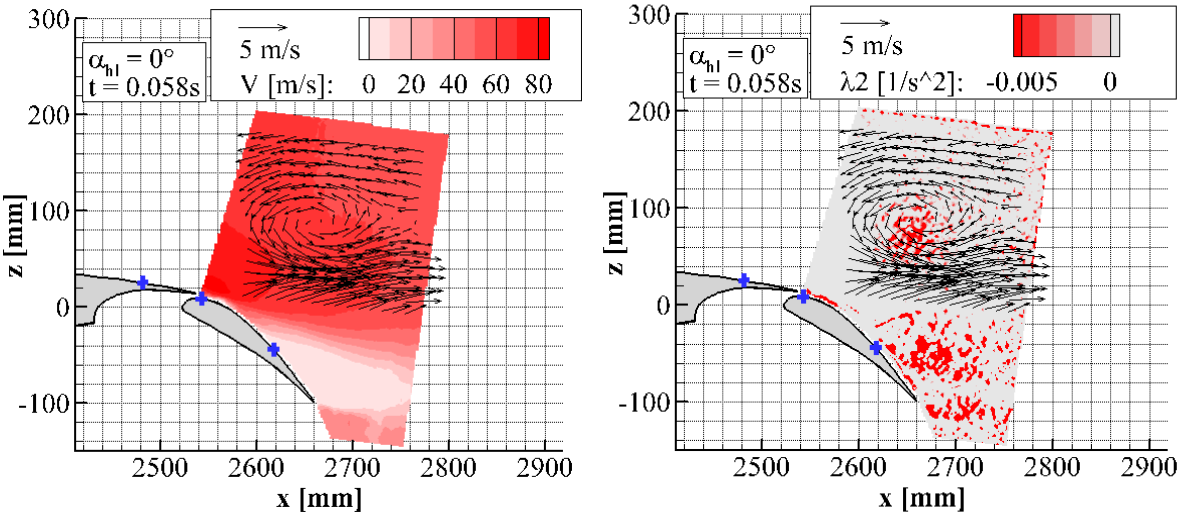

(a) **(b)**

Figure 14. Phase-locked flow field at t = 0.058 s and with $\alpha_{hl} = 0°$. a) The original velocity field $(u,w)^T$ is shown as contour. The vector field results from the "difference vector field method". b) The λ2-criterion is used to identify the vortical structure. The result is presented as background contour. The blue crosses are described in fig. 13.

Coming back to the velocity fields in fig. 13. The time series shows that a vortical structure can be noticed in the measurement region between t = 0.054s and t = 0.060s. The core of the passing vortex seems to appear at time t = 0.058s in the measurement section. This structure was also shown in fig. 11. We compare these results with the findings of fig. 12. The peak disturbances of the main element trailing edge Kulite and the one at the flap leading edge occur at that time when the vortex core is more or less above these Kulites (t = 0.057s). Therefore, these Kulites do not respond to the induced angle of attack, but rather to the induced stream wise velocity. Due to the counter clockwise rotation of the vortex, the velocity induction in stream wise direction is largest underneath the vortex core.

To conclude the behavior of the Kulites along the high-lift airfoil's surface for $\alpha_{hl} = 0°$, we have noticed the following. The main element leading edge experiences the induced angle of attack by the generated vortex. The behavior of the flap trailing edge, being separated under these conditions, is related to the pressure change at the main element leading edge, thus to the circulation change of the main element. Moreover the flap trailing edge reacts faster as the two Kulites located upstream. These two Kulites, located at the main element trailing edge and at the flap leading edge, are mainly disturbed by the induced velocity in stream wise direction. They respond at the time when the vortex is approximately beyond them.

D. Vortex disturbance along the high-lift airfoil for higher angles of attack

In this section, the disturbances are discussed for the two higher angles of attack, $\alpha_{hl} = 6°$ and $\alpha_{hl} = 9°$. Figure 15 shows the reduced pressure time traces of the four Kulites discussed before. First, we focus on the case $\alpha_{hl} = 6°$. As before in fig. 12, the main element trailing edge Kulite and the flap leading edge Kulite show a similar behavior. The start of the disturbance is approximately the same as compared to the case with $\alpha_{hl} = 0°$. Interestingly the two Kulites experience a slight pressure increase in front of their main pressure decrease. These small pressure maxima appear at the same time as the main element leading edge shows its strongest disturbance. Hence, these slightly positive pressure signals result from the induced positive angle of attack that likewise increases the main element's circulation. This positive change in circulation temporarily forces both the main element trailing edge and the flap's leading edge to slightly positive pressures. Moreover their signals are blurred and it takes more time to relax back to the undisturbed level. These phenomena can be linked to viscous effects that are predominant at that range of the angle of attack (see fig. 5). As we now focus on the flap trailing edge Kulite, one notices a pressure increase as for $\alpha_{hl} = 0°$. However, at this angle of attack, its disturbance maximum is located around t = 0.06s. For $\alpha_{hl} = 0°$, this is approximately the time when the generated vortex passes the flap. To verify whether this is likewise the case for $\alpha_{hl} = 6°$ and $\alpha_{hl} = 9°$, respectively, the PIV results are investigated. Figure 16 shows the PIV results at time t = 0.058s for the two angles of attack. The vortex core can be found in the measurement section at the same time as for $\alpha_{hl} = 0°$ in fig. 14. Hence, for $\alpha_{hl} = 6°$, the flap's trailing edge seems to be rather sensitive to the induced velocity of the passing vortex than to the reaction of the

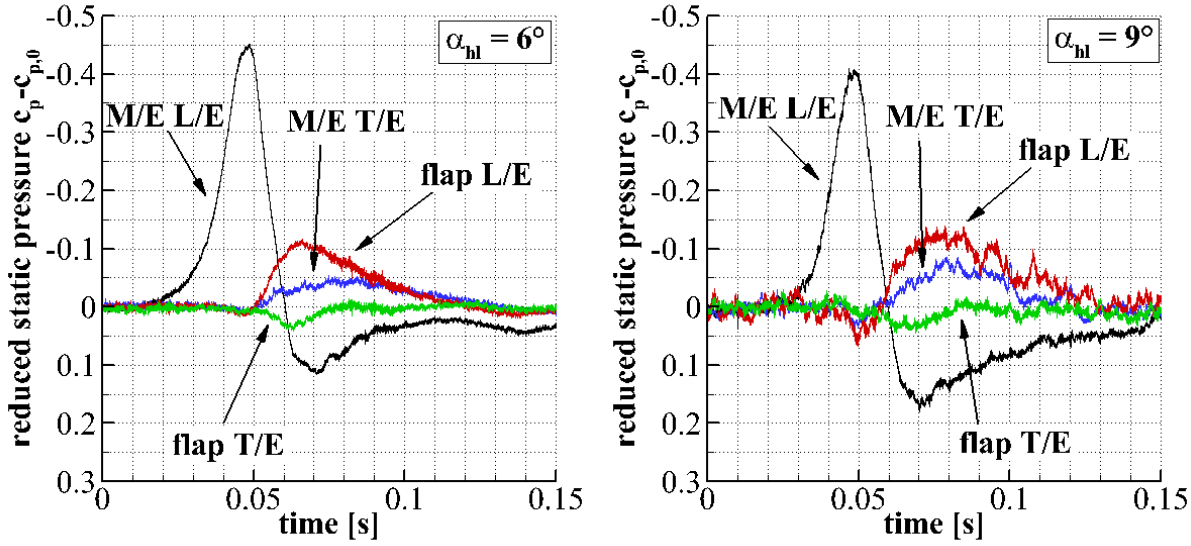

(a) **(b)**

Figure 15. Time traces of the reduced static pressure, $c_p(t)-c_p(t=0)$, of four Kulites along the airfoil's surface for (a) $\alpha_{hl} = 6°$ and (b) $\alpha_{hl} = 9°$. The Kulites are located close to the main element leading edge and trailing edge, so as close to the flap's leading edge and trailing egde. The ensemble averaged data of each Kulite is reduced by its static pressure at time t=0s to allow a better comparison among each other.

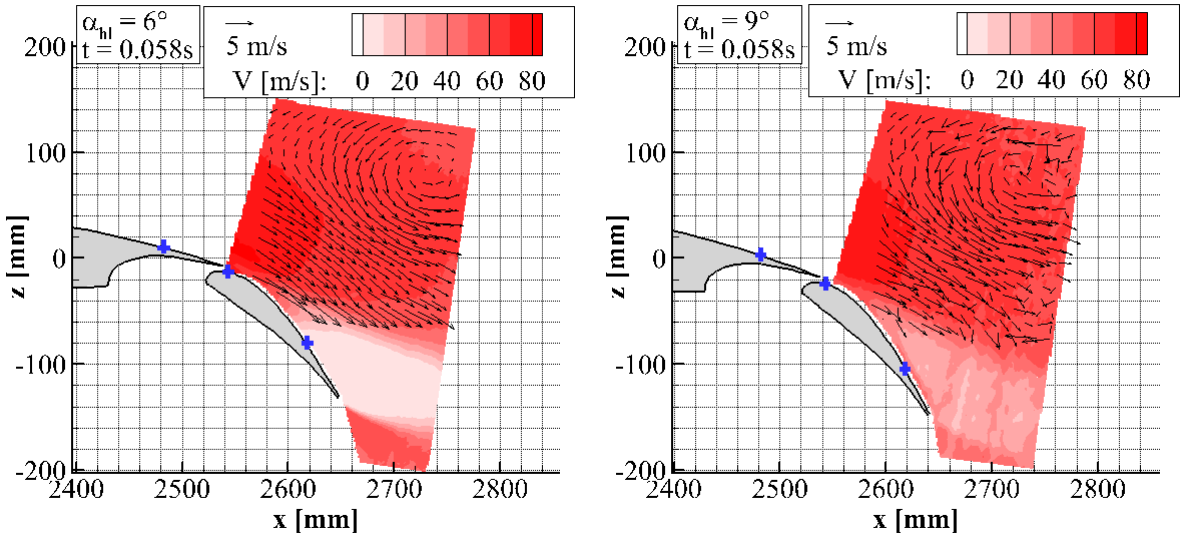

(a) **(b)**

Figure 16. Phase-locked flow field at t = 0.058 s and with (a) $\alpha_{hl} = 6°$ and (b) $\alpha_{hl} = 9°$. Contour plot: original velocity field $(u,w)^T$, Vectors: result from "difference vector field method".

main element leading edge. This difference between the case with $\alpha_{hl} = 0°$ and $\alpha_{hl} = 6°$ could result from the loading of the flap. Since the flap shows an attached flow for $\alpha_{hl} = 6°$, this is assumed to be the reason for the different reaction on the vortex. This implies that the loading of the boundary layer defines whether the flap trailing edge is sensitive to an upstream change in static pressure or to the induced stream wise velocity by the passing vortex.

In fig. 16a, for $\alpha_{hl} = 6°$, an indication of a separation region is still noticeable. This might be due to the fact, that the PIV measurement section is located within a region of local separation (see fig. 7b), since it is located 50mm displaced in lateral direction, parallel to the Kulite section.

For the case of $\alpha_{hl} = 9°$ in fig. 15b, the response of the static pressure on the generated vortex is similar to $\alpha_{hl} = 6°$. The influence of the near stall is visible concerning the fluctuations of the signals. Moreover the signals are even more blurred with respect to $\alpha_{hl} = 6°$. The general trend of either increasing or decreasing static pressure is likewise present. Considering the PIV results in fig. 16b, the flow apparently switches between attached and

separated character. Although fluctuations are present in the measurement, the vortex, respectively the vortex core can be detected.

To summarize these investigations, we have observed that the main element leading edge is sensitive to the change of the angle of attack induced by the generated vortex. The disturbance is rather independent of the absolute angle of attack. Solely, with higher angle of attack, viscous effects seem to delay the relaxation back to the undisturbed level. Compared to that, the main element trailing edge and the flap leading edge are sensitive to the positive velocity in stream wise direction that the passing vortex induces. For $\alpha_{hl} = 0°$, the appearance of the strongest disturbance coincides with the presence of the vortex core beyond these Kulites. For higher angles of attack, their responses are similar, however blurring, due to viscous effects, is noticeable. A slight pressure increase in front of the main disturbance shows the temporary circulation change of the main element. The flap trailing edge shows various effects, depending on the absolute angle of attack. First, it shows a general pressure increase. For $\alpha_{hl} = 0°$ with separated flap flow, it is sensitive to the upstream change of static pressure at the main element leading edge. Its strongest disturbance appears at the same time as for the main element leading edge. This underlines the correspondence between these two Kulites. For $\alpha_{hl} = 6°$ and $\alpha_{hl} = 9°$ the flap is less loaded due to the circulation effect. In these cases, the trailing edge seems mainly sensitive to the induced velocity since its maximum disturbance coincides with the appearance of the vortex core in the measurement section. Finally, we can conclude that the high-lift airfoil responds variably to the induced vortex along its surface. The overall behavior is more or less independent of the absolute angle of attack. Instead, the flap trailing edge reaction strongly depends on the loading of its boundary layer and therefore on the absolute angle of attack.

IV. Conclusion and Outlook

Two-dimensional transversal vortices were chosen to simulate atmospheric up- and down-winds technically in a closed low-speed wind tunnel. These vortices are generated in the wind tunnel test section of the underlying experimental setup by a dynamically pitching, symmetric NACA airfoil. To investigate the complex influence of the generated vortex on the flow of a two-element airfoil in high-lift configuration various measurement techniques were used. The disturbance of the generated vortex on the averaged static pressure distribution along the airfoil's surface was discussed with respect to the distribution for the undisturbed case. The differences between these two distributions were found to be small and simply observable around maximum lift. In this context, the predominant high-lift effects of the present configuration were discussed. The influence of the generated vortex on the time resolving static pressure was studied by accessing the data of four distinct Kulite sensors located along the airfoil's upper surface. Thereby, it was shown, that the main element leading edge is sensitive to the induced angle of attack caused by the leading and trailing flank of the generated vortex. The disturbance on the main element leading edge was found to be rather independent of the angle of attack α_{hl}. By contrast, it could be observed that the main element trailing edge and the flap's leading edge are influenced by the induced, positive velocity in stream wise direction caused by the generated vortex. A complex reaction of the flap trailing edge on the generated vortex was found, depending on the loading of the flap. For the case of heavy loads ($\alpha_{hl} = 0°$), the flap trailing edge is sensitive to the static pressure change at the main element leading edge. With less loaded flap ($\alpha_{hl} = 6°$ and $\alpha_{hl} = 9°$), the flap trailing edge seemed to be likewise sensitive to the induced velocity of the vortex. Moreover, a general trend could be observed. The Kulite signals showed a delay in relaxation back to their undisturbed levels for increasing angle of attack.

Future studies aim at a more detailed investigation of the high-lift airfoil interacting with the generated vortex. Therefore, extended experimental data from Kulite measurements, time-resolving hotfilm measurements at the main element and flap trailing edge as well as measurements of the high-lift airfoil's wake will be analyzed. Moreover, in a further step, more sophisticated disturbances will be produced. Additionally to the existing transversal vortex, a longitudinal vortex will be created. Then, the interaction of these two vortices produces three-dimensional disturbances at the position of the high-lift airfoil. This second, longitudinal vortex will be created by the wing tip vortex of a third, vertically mounted airfoil. This airfoil will be placed in the wind tunnel test section between the vortex generator airfoil and the high-lift airfoil. It will be mounted at the wind tunnel floor with adjustable span. Thus, the height of the longitudinal vortex according to the high-lift airfoil can be varied. Various measurement techniques will be used to establish an extensive database of the interaction of the DLR-F 15 high-lift airfoil with these three-dimensional disturbances.

Acknowledgments

The members of the FOR 1066 research group gratefully acknowledge the support of the "Deutsche Forschungsgemeinschaft DFG" (German Research Foundation) which funded this research.

References

[1]Barlow, J. B., Rae, W. H., and Pope, A., *Low-Speed Wind Tunnel Testing*, 3rd ed., John Wiley & Sons Ltd., New York, 1999.

[2]Freymann, R., „Die Böensimulationsanlage des 3m x 3m – Niedergeschwindigkeitskanals der DFVLR in Göttingen," DFVLR-FB 85-04, 1985.

[3]Hahn, D., Scholz, P., and Radespiel, R., "Experimental evaluation of the stall characteristics of a two-element high lift airfoil," *Second Symposium "Simulation of Wing and Nacelle Stall"*, SFB FOR 1066, Braunschweig, Germany, 2010, https://www.for1066.tu-bs.de/attachments/5-Hahn.pdf.

[4]Hahn, D., Scholz, P., Semaan, R., Radespiel, R., and Müller-Eigner, R., "Erzeugung definierter Querwirbel in einer geschlossenen Messstrecke," *60. Deutscher Luft- und Raumfahrtkongress,* DGLR, Bremen, Germany, 2011.

[5]Hahn, D., Scholz, P., and Radespiel, R., "Vortex generation in a low speed wind tunnel and vortex interactions with a high-lift airfoil," *30th AIAA Applied Aerodynamics Conference*, AIAA, New Orleans, Louisiana, USA, 2012.

[6]Hahn, D., Scholz, P., and Radespiel, R., "Stall behavior of a two-element high-lift airfoil in disturbed flow," *Third Symposium "Simulation of Wing and Nacelle Stall"*, SFB FOR 1066, Braunschweig, Germany, 2012.

[7]Helmke, C., Auerswald, T., Raasch, S., and Bange, J., "Comparison of two methods to provide highly resolved atmospheric turbulence data for simulations of wing and nacelle circulations," *Second Symposium "Simulation of Wing and Nacelle Stall"*, Braunschweig, Germany, 2010, https://www.for1066.tu-bs.de/attachments/12-Helmke.pdf.

[8]Kähler, C. J., Sammler, B., and Kompenhans J., "Generation and control of particle size distributions for optical velocity measurement techniques in fluid mechanics," *Experiments in Fluids*, Vol. 33, 2002, pp. 736–742.

[9]Krag, B., "Vermessung des Böenfeldes hinter harmonisch schwingenden Böenerzeugern im Modell-Unterschall-Kanal (MUK)," Forschungsbericht, Deutsche Forschungs- und Versuchanstalt für Luft- und Raumfahrt , DFVLR-FB 82-26, 1982.

[10]Lee, T., and Gerontakos, P., "Investigation of flow over an oscillating airfoil," *Journal of Fluid Mechanics*, Vol. 512, 2004, pp. 313-341.

[11]Schlichting, H., and Truckenbrodt, E., *Aerodynamik des Flugzeuges*, 2nd ed. , Vol.1 & 2, Springer Verlag, Berlin, 1967

[12]Smith, A.M.O., "High-Lift Aerodynamics," *Journal of Aircraft*, Vol. 12, No. 6, 1975, pp. 501-530.

[13]Swalwell, K. E., Sheridan, J., and Melbourne, W. H., "The Effect of Turbulence Intensity on Stall of the NACA 0021 Airfoil," *14th Australasian Fluid Mechanics Conference*, Adelaide, Australia, 10-14 Dec. 2001.

[14]Wild, J., "Experimental investigation of Mach- and Reynolds-number dependencies of the stall behavior of 2-element and 3-element high-lift wing section," *50th AIAA Aerospace Science Meeting*, Nashville, Tennessee, 09-12 Jan. 2012.